



Aalborg Universitet

AALBORG UNIVERSITY  
DENMARK

## Two-Port Network Modeling and Stability Analysis of Grid-Connected Current-Controlled VSCs

Chou, Shih-Feng; Wang, Xiongfei; Blaabjerg, Frede

*Published in:*  
IEEE Transactions on Power Electronics

*DOI (link to publication from Publisher):*  
[10.1109/TPEL.2019.2934513](https://doi.org/10.1109/TPEL.2019.2934513)

*Publication date:*  
2020

*Document Version*  
Publisher's PDF, also known as Version of record

[Link to publication from Aalborg University](#)

*Citation for published version (APA):*  
Chou, S-F., Wang, X., & Blaabjerg, F. (2020). Two-Port Network Modeling and Stability Analysis of Grid-Connected Current-Controlled VSCs. *IEEE Transactions on Power Electronics*, 35(4), 3519 - 3529. [8794740]. <https://doi.org/10.1109/TPEL.2019.2934513>

### General rights

Copyright and moral rights for the publications made accessible in the public portal are retained by the authors and/or other copyright owners and it is a condition of accessing publications that users recognise and abide by the legal requirements associated with these rights.

- Users may download and print one copy of any publication from the public portal for the purpose of private study or research.
- You may not further distribute the material or use it for any profit-making activity or commercial gain
- You may freely distribute the URL identifying the publication in the public portal -

### Take down policy

If you believe that this document breaches copyright please contact us at [vbn@aub.aau.dk](mailto:vbn@aub.aau.dk) providing details, and we will remove access to the work immediately and investigate your claim.

# Two-Port Network Modeling and Stability Analysis of Grid-Connected Current-Controlled VSCs

Shih-Feng Chou , *Member, IEEE*, Xiongfei Wang , *Senior Member, IEEE*, and Frede Blaabjerg , *Fellow, IEEE*

**Abstract**—Converter-grid interactions tend to bring in frequency-coupled oscillations that deteriorate the grid stability and power quality. The frequency-coupled oscillations are generally characterized by means of multiple-input multiple-output (MIMO) impedance models, which requires using the multivariable control theory to analyze resonances. In this article, instead of the MIMO modeling and analysis, the two-port network theory is employed to integrate the MIMO impedance models into a single-input single-output (SISO) open-loop gain, which is composed by a ratio of two SISO impedances. Thus, the system resonance frequency can be readily identified with Bode plots and the classical Nyquist stability criterion. Case studies in both simulations and experimental tests corroborate the theoretical stability analysis.

**Index Terms**—Impedance model, resonances, stability analysis, two-port network, voltage source converters (VSCs).

## I. INTRODUCTION

VOLTAGE source converters (VSCs) have been widely used in the modern power grid for renewable energy generation, flexible power transmission, and energy-efficient power consumption. As the penetration level of VSCs increases in the power grid, the VSC-grid interactions tend to cause harmonic instability phenomena across a wide frequency range, due to the multitime-scale control dynamics of VSCs [1]. The harmonic instability phenomena are further divided into the frequency-decoupled resonances at harmonic frequencies and the sideband (frequency-coupled) resonances around the grid fundamental frequency [2].

The impedance-based analysis method is commonly used to analyze the system stability and identify the resonance frequency in the frequency-domain [2]. It has been shown that the harmonic resonances are mainly caused by the inner current control loop, where the time delay of the digital control system brings in a negative damping close to the resonance frequencies of passive

filters and grid impedance [3], [4]. Since the inner control loop has symmetric dynamics in the  $dq$ - or  $\alpha\beta$ -frame, it can be represented by two single-input single-output (SISO) transfer functions or one complex transfer function [3], [5], and thus the resonance frequency can be readily identified in Bode plots based on the Nyquist stability criterion.

In contrast, the sideband resonances of the fundamental frequency [6]–[14], which are resulted from the asymmetric  $dq$ -frame dynamics of the phase-locked loop (PLL) [6]–[11], and the outer power control loops, e.g., the constant power load with the regulated dc-link voltage loop [12], [13], or the alternative voltage magnitude control loop [14]. In those cases, the negative damping are introduced at either  $d$ - or  $q$ -axis, instead of symmetrically on both  $d$ - and  $q$ -axes. Consequently, the sideband resonances cannot be simply modeled by SISO transfer functions [5], and the multiple-input multiple-output (MIMO) transfer function matrices are needed to characterize the frequency-coupling dynamics [10]–[12].

There are two general approaches for developing the MIMO impedance matrices in respect to the used reference frame, i.e., the  $dq$ -frame impedance matrices [6]–[8], [13] and the  $\alpha\beta$ -frame impedance matrices [9]–[12]. The mathematical relationships between the two reference-frame impedance matrices has been explicitly revealed in [10], and the same stability implications of two impedance matrices have been proved. An important difference between two impedance matrices is that the  $dq$ -frame impedance matrices are derived based on the linear time-invariant (LTI) operating points, where the dynamic couplings between different frequencies in the phase domain are hidden in the  $dq$ -frame [6]–[8], whereas the  $\alpha\beta$ -frame impedance matrices are essentially developed based on the linear time-periodic operating trajectories [2], [10], [11], which enables to directly capture the frequency-coupling dynamics. However, both impedance matrices are MIMO systems, which require using the generalized (multivariable) Nyquist stability criterion to predict the system stability, and the Bode plots of the eigenvalues of the MIMO return-ratio matrix were drawn to identify resonance frequencies of the marginally stable system, yet they provide little insight into how the grid impedance affect the system resonance frequencies in [12]. Therefore, two SISO impedances derived in the  $\alpha\beta$ -frame, which are known as the sequence-domain impedance model, were used to predict the system stability in [9], yet the method overlooks the nonzero off-diagonal elements in the derived impedance matrix, which implies the frequency-coupling dynamics were not considered and the inaccurate stability implication may be resulted [10]–[12].

Manuscript received December 12, 2018; revised March 19, 2019 and June 13, 2019; accepted August 6, 2019. Date of publication August 11, 2019; date of current version January 10, 2020. This work was supported in part by the Reliable Power Electronic-Based Power System (REPEPS) Project at the Department of Energy Technology, Aalborg University, as a part of the Villum Investigator Program funded by the Villum Foundation. Recommended for publication by Associate Editor F. H. Khan. (*Corresponding author: Xiongfei Wang.*)

The authors are with the Department of Energy Technology, Aalborg University, Aalborg 9220, Denmark (e-mail: shc@et.aau.dk; xwa@et.aau.dk; fbl@et.aau.dk).

Color versions of one or more of the figures in this article are available online at <http://ieeexplore.ieee.org>.

Digital Object Identifier 10.1109/TPEL.2019.2934513

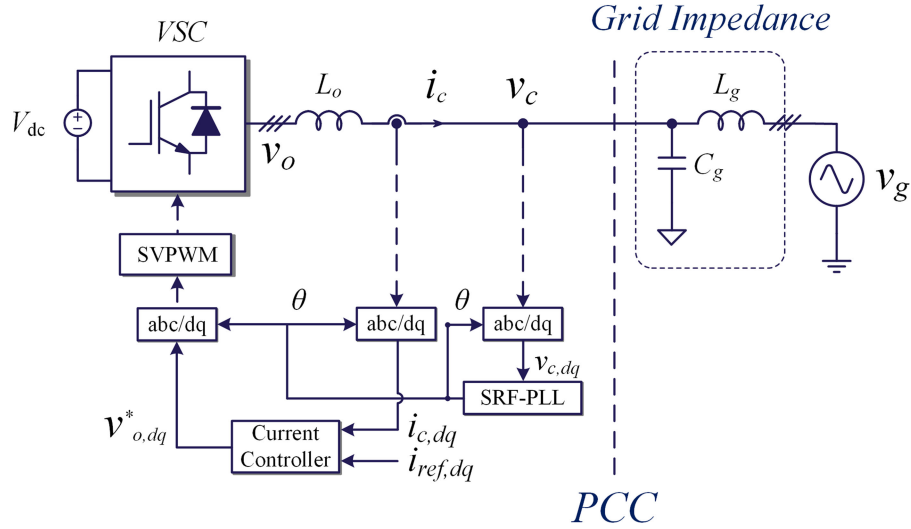


Fig. 1. Single-line diagram of a three-phase grid-connected VSC with current control and SRF-PLL.

In order to avoid using the generalized Nyquist stability criterion, a method based on the MIMO closed-loop transfer function matrix of the entire system is recently introduced in [14]. In the approach, instead of deriving the MIMO impedance matrix describing the VSC terminal behaviors, the MIMO closed-loop transfer function matrix of the entire system is derived considering the impacts of the PLL, the inner current control loop, and the outer power control loops along with the grid impedance. It is then found that the SISO transfer function entries of the MIMO closed-loop transfer matrix share a common denominator, from which a SISO open-loop gain is extracted for predicting the system stability based on the classical stability criterion. A prominent feature of this method is that the design-oriented stability analysis can be performed based on the SISO transfer functions, i.e., how do controller parameters affect the overall system stability can be characterized. However, the VSC-grid interactions are implicitly exposed since the grid impedance is embedded in the MIMO closed-loop transfer function matrix of the entire system. Furthermore, the derivation of the SISO transfer function in [14] is nontrivial due to the dynamic coupling between different control loops.

In this article, instead of analytically deriving the common SISO open-loop gain of the MIMO system for stability analysis, the two-port network theory that is used for analyzing large-scale integrated circuits [15] is applied to the impedance-based modeling method to reorganize the MIMO impedance matrices of the VSC and the grid impedance, where the common SISO open-loop gain is then directly derived with the output admittances at the terminals of the VSC and the grid impedance. Therefore, there is thus no need of prior knowledge on system parameters, and the common SISO open-loop gain can be even derived with the black box models of grid-connected VSCs, which, consequently, provide a more efficient and intuitive method than that in [14]. Moreover, based on the two-port impedance network, the common SISO open-loop gain can be further transformed into two SISO impedance ratios seen from the network terminals, and the VSC-grid interactions can be separately analyzed on each

terminal. Therefore, only the equivalent admittances seen from the terminals is required, and the measurements of the entire MIMO impedance matrices are avoided [16], which significantly facilitates the stability analysis and the resonance frequencies caused by the asymmetric  $dq$ -frame control dynamics can be readily identified with the Bode plots of SISO impedance ratios. Simulations and experimental tests validate the effectiveness of the proposed stability analysis method.

## II. GRID-CONNECTED VSCs

In this section, the derivation of the  $\alpha\beta$ -frame impedance model for a current-controlled grid-connected VSC with the effect of PLL [10] is reviewed, which provides a basis for utilizing the two-port network theory in the next section.

### A. System Description

Fig. 1 illustrates a single-line diagram of a three-phase grid-connected current-controlled VSC, where a stiff dc voltage source  $V_{dc}$  is used. Similar to [6]–[11], the frequency-coupled resonance caused from the synchronous reference frame (SRF)-PLL [17] is focused in this article. The L-filter is used at the ac side, and an  $LC$ -resonant grid impedance is considered at the point of common coupling (PCC), including a grid inductance  $L_g$  and a capacitance  $C_g$ . The PCC voltage, i.e., the voltage across the filter capacitor  $v_c$  is measured by the SRF-PLL for the grid synchronization purpose.

### B. $dq$ -Frame Impedance Modeling

The current controller is implemented in the  $dq$ -frame, whose dynamic is thus affected by the phase angle  $\theta$  measured by the SRF-PLL [5]. Considering the dynamic effect of the SRF-PLL, the small-signal block diagram of the current control loop in the  $dq$ -frame can be drawn in Fig. 2, which has been explicitly derived in [2].

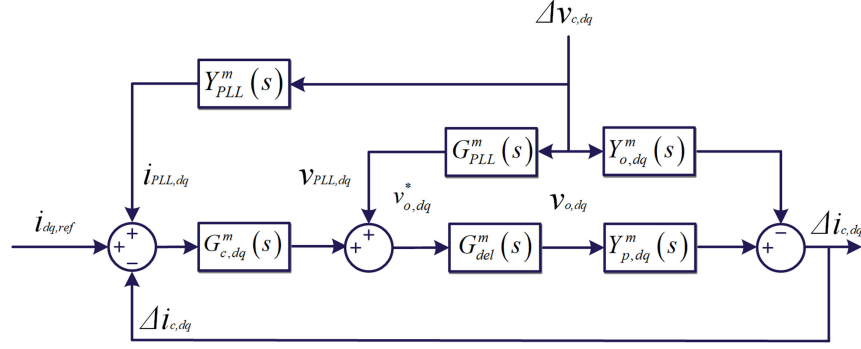


Fig. 2. Small-signal block diagram of the current control loop with the effect of SRF-PLL in the  $dq$ -frame.

The superscript “ $m$ ” in the block of Fig. 2 implies the MIMO transfer function matrix, instead of SISO transfer functions. In Fig. 2,  $Y_{p,dq}^m(s)$  and  $Y_{o,dq}^m(s)$  illustrate the  $L$ -filter plant.  $G_{c,dq}^m(s)$  and  $G_{del}^m(s)$  are diagonal matrices, where  $G_{c,dq}^m(s)$  represents the PI current controller transfer function matrix with the proportional gain  $K_{cp}$  and the integral gain  $K_{ci}$ , and  $G_{del}^m(s)$  denotes the time delay, which is introduced by the digital computation ( $T_s$ ) and the pulse width modulation ( $0.5T_s$ ) [18], where  $T_s$  is the sampling period.  $Y_{PLL}^m(s)$  and  $G_{PLL}^m(s)$  represent the dynamic effect of the SRF-PLL, through the Park- and the inverse Park-transformations on the current  $\Delta i_{c,dq}$  and the voltage command  $v_{o,dq}^*$ , respectively.  $Y_{PLL}^m(s)$  and  $G_{PLL}^m(s)$  are given as

$$Y_{PLL}^m(s) = \begin{bmatrix} 0 & -H_{PLL}(s)V_{c,q} \\ 0 & H_{PLL}(s)V_{c,d} \end{bmatrix} \quad (1)$$

$$G_{PLL}^m(s) = \begin{bmatrix} 0 & -H_{PLL}(s)I_{c,q} \\ 0 & H_{PLL}(s)I_{c,d} \end{bmatrix} \quad (2)$$

where  $H_{PLL}(s)$  is the small-signal model of the SRF-PLL [17], which is linearized as a second-order dynamic system [3]. From Fig. 2, the reference-to-output transfer function matrix,  $G_{cl,dq}^m(s)$  and the closed-loop output admittance matrix,  $Y_{cl,dq}^m(s)$  can be derived, respectively, as

$$\underbrace{\begin{bmatrix} \Delta i_{c,d} \\ \Delta i_{c,q} \end{bmatrix}}_{\Delta i_{c,dq}} = G_{cl,dq}^m(s) \underbrace{\begin{bmatrix} i_{d,ref} \\ i_{q,ref} \end{bmatrix}}_{i_{dq,ref}} + Y_{cl,dq}^m(s) \underbrace{\begin{bmatrix} \Delta v_{c,d} \\ \Delta v_{c,q} \end{bmatrix}}_{\Delta v_{c,dq}} \quad (3)$$

where  $G_{cl,dq}^m(s)$  is given by

$$G_{cl,dq}^m(s) = [I^m + T_{dq}^m(s)]^{-1} T_{dq}^m(s) \quad (4)$$

where  $T_{dq}^m(s)$  is the open-loop gain of the transfer function matrix, which is given by

$$T_{dq}^m(s) = Y_{p,dq}^m(s) G_{del,dq}^m(s) G_{c,dq}^m(s) \quad (5)$$

The closed-loop output admittance matrix,  $Y_{cl,dq}^m(s)$ , denotes the disturbance (the PCC voltage)-to-output transfer function,

and it can be derived as [7]

$$\begin{aligned} Y_{cl,dq}^m(s) &= G_{cl,dq}^m(s) Y_{PLL}^m(s) \\ &+ [I^m + T_{dq}^m(s)]^{-1} Y_{p,dq}^m(s) G_{del,dq}^m(s) G_{PLL}^m(s) \\ &- [I^m + T_{dq}^m(s)]^{-1} Y_{o,dq}^m(s). \end{aligned} \quad (6)$$

As given by (1) and (2),  $Y_{PLL}^m(s)$  and  $G_{PLL}^m(s)$  are asymmetric matrices, which make  $Y_{cl,dq}^m(s)$  asymmetric, and thus it cannot be analyzed as SISO complex transfer functions [5].

### C. $\alpha\beta$ -Frame Impedance Modeling

The  $dq$ -frame impedance matrix derived in (6) is based on real vectors which is LTI, and thus it cannot explicitly disclose the dynamic couplings between different frequencies in the phase domain. Thus, the transformation from a general real-valued transfer function matrix to its equivalent based on complex vectors, yet still in the  $dq$ -frame, has been earlier introduced in [19]. This transformation matrix is recently applied to the  $dq$ -frame impedance matrix in [8], while in [2], this transformation is derived from the complex transfer function equivalent of an asymmetric transfer function matrix, which is summarized and shown in Fig. 3.  $y_{+,dq}^*(s)$  and  $y_{-,dq}^*(s)$  are the complex conjugates of the complex transfer functions  $y_{+,dq}(s)$  and  $y_{-,dq}(s)$ , respectively. Hence, the frequency coupling dynamics caused by asymmetric control loops in the  $dq$ -frame are implanted into the system.

Then, considering the frequency translation between the  $dq$ - and  $\alpha\beta$ -frame, the  $\alpha\beta$ -frame complex-valued impedance matrix can be derived as [10]

$$\begin{bmatrix} \Delta i_{c,\alpha\beta} \\ e^{j2\theta} \Delta i_{c,\alpha\beta}^* \end{bmatrix} = \underbrace{\begin{bmatrix} y_+(s) & y_-(s) \\ y_-^*(s) & y_+^*(s) \end{bmatrix}}_{Y_{\pm cl}^m(s)} \begin{bmatrix} \Delta v_{c,\alpha\beta} \\ e^{j2\theta} \Delta v_{c,\alpha\beta}^* \end{bmatrix} \quad (7)$$

where  $Y_{\pm cl}^m(s)$  shows the electrical relations of complex vectors at different frequencies, and  $\Delta v_{c,\alpha\beta}^*$  is the complex conjugate vector of  $\Delta v_{c,\alpha\beta}$  in the  $\alpha\beta$ -frame. For a given voltage vector at the frequency  $\omega$ , a frequency-coupled current vector at the frequency  $2\omega_1 - \omega$  is generated according to (7), where  $\omega_1$  is the grid fundamental frequency. It is worth mentioning that the  $\alpha\beta$ -frame impedance (or admittance) matrix has been validated

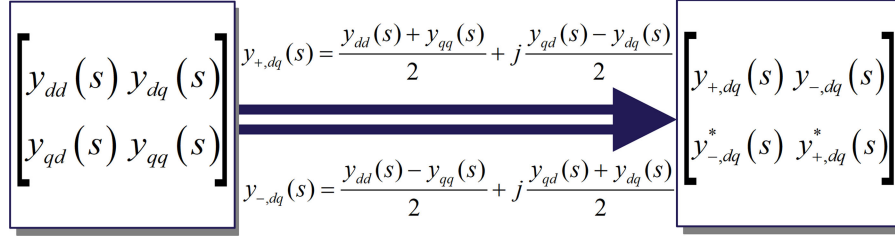


Fig. 3. Complex transfer function equivalent of an asymmetric transfer function matrix.

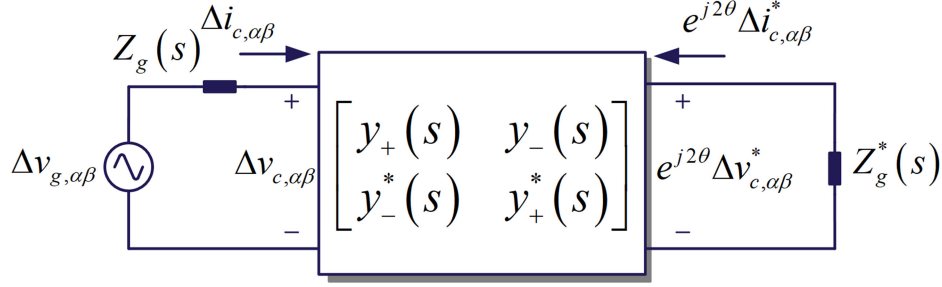


Fig. 4. General two-port network representation of a grid-connected VSC based on impedance matrices.

in [10], and the model validation will not be repeated in this article.

### III. TWO-PORT NETWORK FOR STABILITY ANALYSIS

This section presents first a general two-port network representation of grid-connected VSCs based on the MIMO impedance matrices, and then elaborates the principle of deriving the common SISO open-loop gain from the two-port network. The essential differences between the proposed approach and the conventional impedance-based stability analysis method are highlighted.

#### A. General Two-Port Network Representation

Fig. 4 illustrates a general two-port network representation of grid-connected VSCs based on the MIMO impedance matrices, where the grid impedance matrix in the  $\alpha\beta$ -frame is diagonal, which is expressed as [10], [11]

$$\begin{bmatrix} \Delta v_{c,\alpha\beta} \\ e^{j2\theta} \Delta v_{c,\alpha\beta}^* \end{bmatrix} = \begin{bmatrix} \Delta v_{g,\alpha\beta} \\ e^{j2\theta} \Delta v_{g,\alpha\beta}^* \end{bmatrix} - \underbrace{\begin{bmatrix} Z_g(s) & 0 \\ 0 & Z_g^*(s) \end{bmatrix}}_{Z_g^m(s)} \begin{bmatrix} \Delta i_{c,\alpha\beta} \\ e^{j2\theta} \Delta i_{c,\alpha\beta}^* \end{bmatrix}. \quad (8)$$

In order to preserve the physical property at the PCC of VSC and meanwhile illustrate the frequency-coupling dynamics, the two grid impedance entries are distributed on two ports of the network.

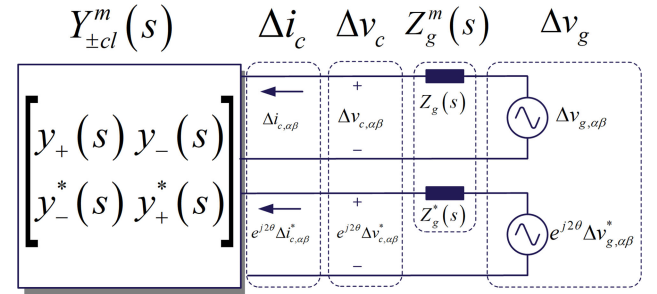


Fig. 5. Impedance equivalent model of the current-controlled grid-connected VSC.

#### B. Conventional Impedance-Based Stability Analysis

In the conventional impedance-based approach, the grid impedance matrix is cascaded with the VSC admittance matrix as shown in Fig. 5, and the open-loop transfer function matrix of the MIMO system is derived directly from the ratio of impedance matrices, i.e., the return-ratio matrix  $L_m(s)$ , which is given by

$$L_m(s) = Z_g^m(s) Y_{\pm,cl}^m(s). \quad (9)$$

Then the generalized Nyquist stability criterion is applied to the return-ratio matrix for the stability prediction. This is basically a MIMO system analysis method, and has been widely used with three-phase VSC systems [6]–[13]. To utilize this method, all entries of the impedance matrices need to be known, either by analytical derivations or through impedance measurements [16]. Moreover, the Nyquist plots of eigenvalues of the return-ratio matrix provide little insight into how the grid impedance affect the system resonance frequency [14].



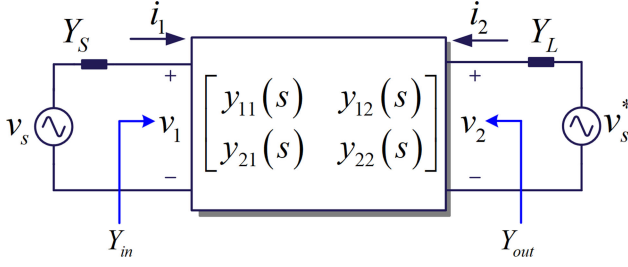


Fig. 6. General admittance form LTI two-port network model.

### C. Proposed Stability Analysis Method

Instead of utilizing the multivariable control theory, the active network analysis theory [20] is employed to analyze the VSC-grid interactions. Given a general LTI two-port network model constituted by admittance matrices, which is shown in Fig. 6, the dynamic interactions at each port can be analyzed by applying the superposition principle and using the SISO impedances seen from each port, which are illustrated as follows.

First, considering the input voltage  $v_s$  only and  $v_s^*$  is set to zero, the current at Port 2 can be derived as

$$i_2 = -v_2 Y_L \quad (10)$$

and the electrical relations of the two-port network is shown as

$$\begin{bmatrix} i_1 \\ i_2 \end{bmatrix} = \begin{bmatrix} y_{11} & y_{12} \\ y_{21} & y_{22} \end{bmatrix} \begin{bmatrix} v_1 \\ v_2 \end{bmatrix}. \quad (11)$$

Substituting (10) into (11), the following transfer functions can be derived

$$G_v = \frac{v_2}{v_1} = \frac{-y_{21}}{y_{22} + Y_L} \quad (12)$$

$$Y_{in} = \frac{i_1}{v_1} = y_{11} + y_{12} \frac{v_2}{v_1} = y_{11} - \frac{y_{12}y_{21}}{y_{22} + Y_L} \quad (13)$$

where  $G_v$  is the internal two-port gain, and  $Y_{in}$  is the equivalent input admittance seen from the Port 1. Then, including the admittance  $Y_S$ , the SISO closed-loop gain from  $v_s$  to  $v_1$  can be derived as

$$\frac{v_1}{v_s} = \frac{\frac{Y_S}{Y_S + y_{11}}}{1 - \frac{y_{12}y_{21}}{(Y_S + y_{11})(Y_L + y_{22})}}. \quad (14)$$

Based on (12) and (14), the SISO closed-loop gain from  $v_s$  to  $v_2$  can then be calculated as

$$\frac{v_2}{v_s} = \frac{v_2}{v_1} \frac{v_1}{v_s} = -\frac{\frac{y_{21}Y_S}{(Y_S + y_{11})(Y_L + y_{22})}}{1 - \frac{y_{12}y_{21}}{(Y_S + y_{11})(Y_L + y_{22})}}. \quad (15)$$

Next, considering the input voltage  $v_s^*$  only and setting  $v_s$  as zero, the SISO closed-loop gains from  $v_s^*$  to  $v_1$  and  $v_2$  can be

derived similarly, which are given by

$$\frac{v_1}{v_s^*} = -\frac{\frac{y_{12}Y_L}{(Y_S + y_{11})(Y_L + y_{22})}}{1 - \frac{y_{12}y_{21}}{(Y_S + y_{11})(Y_L + y_{22})}} \quad (16)$$

$$\frac{v_2}{v_s^*} = \frac{\frac{Y_L}{Y_L + y_{22}}}{1 - \frac{y_{12}y_{21}}{(Y_S + y_{11})(Y_L + y_{22})}}. \quad (17)$$

From (14)–(17), it is clear that all the SISO closed-loop gains share the same characteristic equation, and a common open-loop gain  $G_L$  can be identified from that, which is given by

$$G_L = -\frac{y_{12}y_{21}}{(Y_S + y_{11})(Y_L + y_{22})}. \quad (18)$$

Then, the stability of the two-port network can be evaluated based on (18), which, differs from the conventional impedance-based approach, is a SISO transfer function. Thus, the classical Nyquist stability criterion can be applied, which significantly simplifies the stability analysis and the system resonance frequency can be readily identified through the Bode plots of (18).

It is worth mentioning that the concept of the common SISO open-loop gain has been introduced in [14] for the stability analysis of grid-connected VSCs. However, instead of utilizing the impedance-based representation, the common SISO open-loop gain given in [14] is analytically derived from a closed-loop MIMO transfer function matrix of the entire system, which contains the VSC with the predefined control structure and controller parameters along with the grid impedance. Moreover, the whole computation process is more complicated than Fig. 6.

In addition, although the SISO open-loop gain given in (18) is based on admittance matrices, it requires knowing all the entries of the admittance matrices, similarly to the conventional impedance-based approach. It is shown that measuring all the entries of the  $\alpha\beta$ -frame admittance matrix is difficult, yet the measurement of the equivalent terminal admittances can be readily obtained. Hence, a refined frequency scan approach that considers the frequency coupling dynamics of VSCs is introduced in [16]. Thus, to deal with this challenge, the SISO closed-loop gains are reformulated as follows:

$$\frac{v_1}{v_s} = \frac{Y_S}{Y_S + Y_{in}} = \frac{\frac{Y_S}{Y_{in}}}{1 + \frac{Y_S}{Y_{in}}} \quad (19)$$

$$\frac{v_2}{v_s} = G_v \frac{Y_S}{Y_S + Y_{in}} = G_v \frac{\frac{Y_S}{Y_{in}}}{1 + \frac{Y_S}{Y_{in}}} \quad (20)$$

$$\frac{v_1}{v_S^*} = G_v^* \frac{Y_L}{Y_L + Y_{out}} = G_v^* \frac{\frac{Y_L}{Y_{out}}}{1 + \frac{Y_L}{Y_{out}}} \quad (21)$$

$$\frac{v_2}{v_S^*} = \frac{Y_L}{Y_L + Y_{out}} = \frac{\frac{Y_L}{Y_{out}}}{1 + \frac{Y_L}{Y_{out}}} \quad (22)$$

where

$$G_v^* = \frac{-y_{12}}{y_{11} + Y_S}. \quad (23)$$

It is seen that the SISO open-loop gain can be reformulated as two impedance ratios, where  $Y_{out}$  is the equivalent output admittance seen from Port 2, which is given as

$$Y_{out} = y_{22} - \frac{y_{12}y_{21}}{y_{11} + Y_S}. \quad (24)$$

Thus, instead of identifying all the entries of the admittance matrix, only the equivalent input and output admittances at the Port 1 and Port 2 are required for the stability analysis.

Following this principle, the general two-port network model shown in Fig. 6 can be replaced by that shown in Fig. 4, and then the corresponding equivalent admittances can be derived as

$$Y_S = \frac{1}{Z_g(s)} \quad (25)$$

$$Y_L = \frac{1}{Z_g^*(s)} \quad (26)$$

$$Y_{in} = y_+(s) - \frac{y_-(s)y_+^*(s)}{\left(y_+^*(s) + \frac{1}{Z_g^*(s)}\right)} \quad (27)$$

$$Y_{out} = y_+^*(s) - \frac{y_-(s)y_-^*(s)}{\left(y_+(s) + \frac{1}{Z_g(s)}\right)}. \quad (28)$$

#### IV. CASE STUDIES AND VERIFICATIONS

In order to validate the effectiveness of the proposed stability analysis method, four different cases based on the system diagram shown in Fig. 1 are studied in this section, including the frequency-domain stability analysis, time-domain simulations and experimental verifications. In experimental tests, the experimental platform is shown in Fig. 7 that a constant dc voltage source is used at the dc-side of the VSC, and a regenerative grid simulator is used to emulate the grid voltage. The digital control system of the VSC is implemented in the dSPACE DS1007 system, where the voltage and current are measured by using the DS2004 high-speed A/D board, and the gate signals are generated using DS5101 digital waveform output board.

*Descriptions of Cases:* Tables I–III provide the electrical system and controller parameters used in the four cases, where the same current controller parameters are used, yet different PLL parameters are compared. Moreover, to evaluate the stability of VSC under weak grid conditions, four different grid inductances yet the same grid capacitance, corresponding to

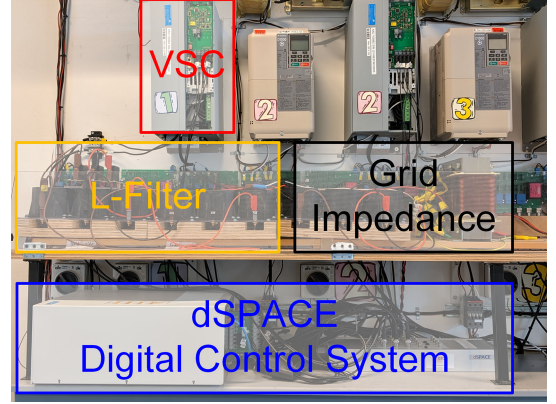


Fig. 7. Configuration of the experimental platform.

TABLE I  
IDENTICAL SYSTEM PARAMETERS USED IN THE FOUR CASES

| System symbol   | Parameter Description         | Value       |
|-----------------|-------------------------------|-------------|
| $V_{dc}$        | Dc bus voltage                | 650 V       |
| $I_{d,cmd}$     | Current command in d-axis     | 21.2 A      |
| $f_{sw}$        | Switching frequency           | 10 kHz      |
| $T_s$           | Sampling time                 | 100 $\mu$ s |
| $K_{cp}/K_{ci}$ | Current controller parameters | 7.9 / 2742  |
| $L_o$           | Converter side inductor       | 1.5 mH      |
| $C_g$           | Grid capacitor                | 15 $\mu$ F  |

different short-circuit ratio (SCR) values are considered, and the  $q$ -axis current commands are adjusted in order to compensate the voltage drop caused by the grid inductance variation.

First, a reference case is introduced in *Case I*, where the VSC is tested with the SCR of 2.5, the  $d$ -axis current command is equal to 21.2 A, and the  $q$ -axis current command is set as  $-4.5$  A. The proportional gain used in the SRF-PLL  $K_{pp}$  is designed as 1.05 [17]. Then, in the *Case II*, a lower bandwidth of SRF-PLL than that in *Case I* is tested, and hence all the parameters are the same as *Case I*, expect that  $K_{pp}$  is set as 0.35. Next, in *Case III*, a weaker grid condition with the SCR of 1.6 is tested, which corresponds to an increase of the grid inductance from 11 to 16.4 mH, and accordingly, the  $q$ -axis current command is tuned from  $-4.5$  to  $-7.2$  A. The other parameters are the same as *Case I*. Lastly, a different grid voltage amplitude, i.e.,  $400 V_{rms}$ , is considered in the *Case IV*, yet the grid inductance remains unchanged from *Case I*, and thus the SCR is increased from 2.5 to 4.4, and the  $q$ -axis current command is changed from  $-4.5$  to  $-2$  A.

It is important to note that in all cases, the integral gain of the SRF-PLL,  $K_{pi}$ , is tuned to make the system marginally stable in simulations and experiments. Due to the nonidealities in the experimental setup, the critical PLL parameters that cause the system marginally stable are slightly different between simulations and experiments in the four cases (see Table III), and consequently the resulted resonance frequencies are also shifted with the maximum 1.5 Hz.

TABLE II  
DIFFERENT SYSTEM PARAMETERS USED IN THE FOUR CASES

| System symbol | $V_{g,rms}$  | $I_{q,cmd}$               | $K_{pp}$                     | $SCR (L_g)$                           |
|---------------|--------------|---------------------------|------------------------------|---------------------------------------|
|               | Grid Voltage | Current command in q-axis | Proportional gain in SRF-PLL | Short Circuit Ratio (Grid Inductance) |
| Case I        | 220 V, 50 Hz | -4.5 A                    | 1.05                         | 2.5 (11.0 mH)                         |
| Case II       | 220 V, 50 Hz | -4.5 A                    | 0.35                         | 2.5 (11.0 mH)                         |
| Case III      | 220 V, 50 Hz | -7.2 A                    | 1.05                         | 1.6 (16.4 mH)                         |
| Case IV       | 400 V, 50 Hz | -2.0 A                    | 1.05                         | 4.4 (11.0 mH)                         |

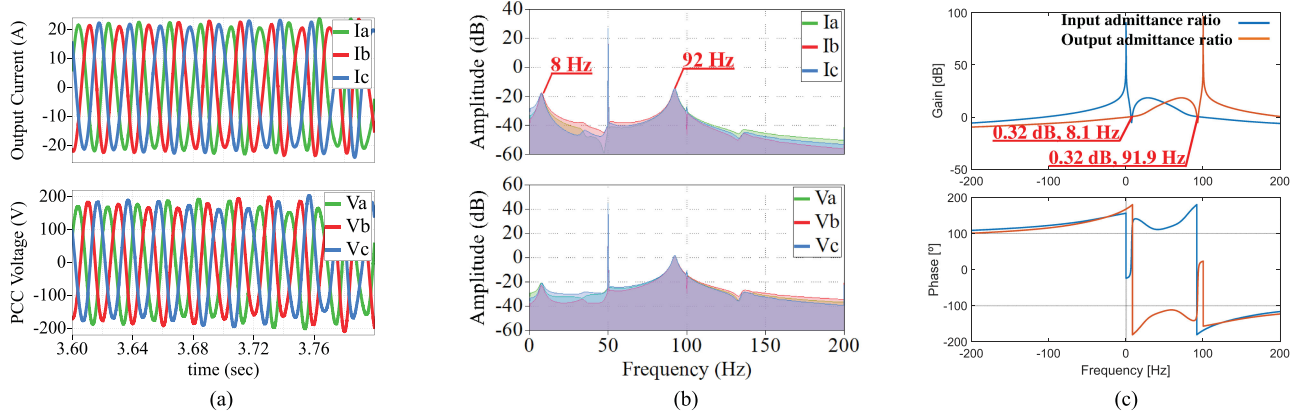


Fig. 8. Simulation result and frequency-domain analysis for Case I. (a) Converter output current and PCC voltage waveform. (b) Frequency spectrum of (a). (c) Bode plot of input and output admittance ratios.

TABLE III  
INTEGRAL GAIN  $K_{pi}$  USED IN SRF-PLL WHERE INSTABILITY OCCURS

|          | Simulation | Experiment |
|----------|------------|------------|
| Case I   | 237        | 216        |
| Case II  | 128        | 117        |
| Case III | 59         | 56         |
| Case IV  | 285        | 285        |

*Case I – Reference Case:* Fig. 8 shows the simulation results and the associated frequency-domain analysis for the *Case I*, where the integral gain of the SRF-PLL  $K_{pi}$  is identified as 237 to make the system marginally stable in simulations. Fig. 8(a) show the simulated VSC current and PCC voltage waveforms. However, the resonance frequencies are hidden in the time-domain simulation. The corresponding harmonic spectrum is given in Fig. 8(b), where the frequency resolution is set as 0.5 Hz in both simulations and experiments. It is clear that the resonance frequencies are 8 and 92 Hz. Then, Fig. 8(c) shows the Bode plots of the admittance ratios derived in (19)–(22). It can be seen that the magnitude response of the input admittance ratio  $\frac{Y_S}{Y_{in}}$  reaches 0.32 dB at the phase crossover frequency (91.9 Hz), which implies the gain margin of 0.32 dB, and meanwhile the output admittance ratio  $\frac{Y_L}{Y_{out}}$  also reaches 0.32 dB at the phase crossover frequency (8.1 Hz). Both of them match well with the

resonance frequencies of 92 and 8 Hz identified in the harmonic spectra analysis as shown in Fig. 8(b).

Fig. 9 shows the experimental results and the associated frequency-domain analysis for the *Case I*. Differs from the simulation, the system encounters resonance when  $K_{pi}$  is 216, which is less than that in the simulation. The resonance frequencies are also shifted with 1.5 Hz, as shown by the harmonic spectra in Fig. 9(b). Fig. 9(c) shows the frequency-domain analysis result with the  $K_{pi}$  used in the experiment. It is clear that the gain margin of two admittance ratios is increased to 0.72 dB, due to the reduced  $K_{pi}$ , and the phase crossover frequencies are indicated as 9.3 and 90.7 Hz. Hence, even though the PLL parameters are slightly different between the simulation and the experiment, the proposed method predicts well the resonance frequencies by means of two SISO admittance ratios, which greatly facilitate the system stability analysis compared to the conventional impedance-based approach.

*Case II – Lower SRF-PLL Bandwidth:* Fig. 10 shows the simulation result and the frequency-domain analysis for the *Case II*. In this case, the proportional gain of the SRF-PLL,  $K_{pp}$  is intentionally reduced to obtain a lower bandwidth, as given by Table II, and then  $K_{pi}$  is found to be 128 when the system becomes marginally stable. From the harmonic spectra analysis in Fig. 10(b), it can be seen that the resonance frequencies are 24.5 and 75.5 Hz, which are higher than the *Case I*. This is because the reduced bandwidth of SRF-PLL leads to a lower-frequency oscillation at the  $q$ -axis [7], which leads to the frequency-coupled resonances at a higher frequency in the  $\alpha\beta$ -frame [10], i.e.,



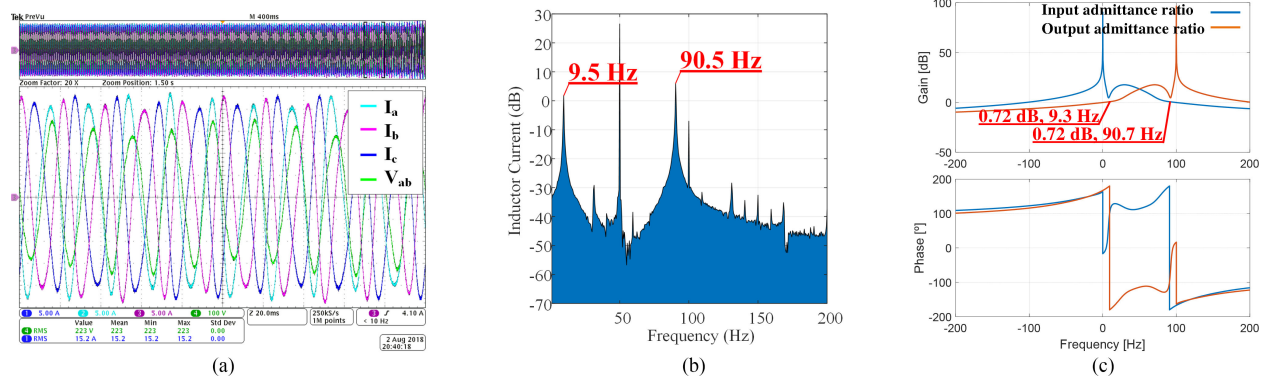


Fig. 9. Experimental result and frequency-domain analysis for Case I. (a) Converter output current and PCC voltage waveform (X-axis: 20 ms/div, Y-axis:  $I_a$ ,  $I_b$ ,  $I_c$ : 5 A/div,  $V_{ab}$ : 100 V/div). (b) Frequency spectrum of converter output current in (a). (c) Bode plot of input and output admittance ratios.

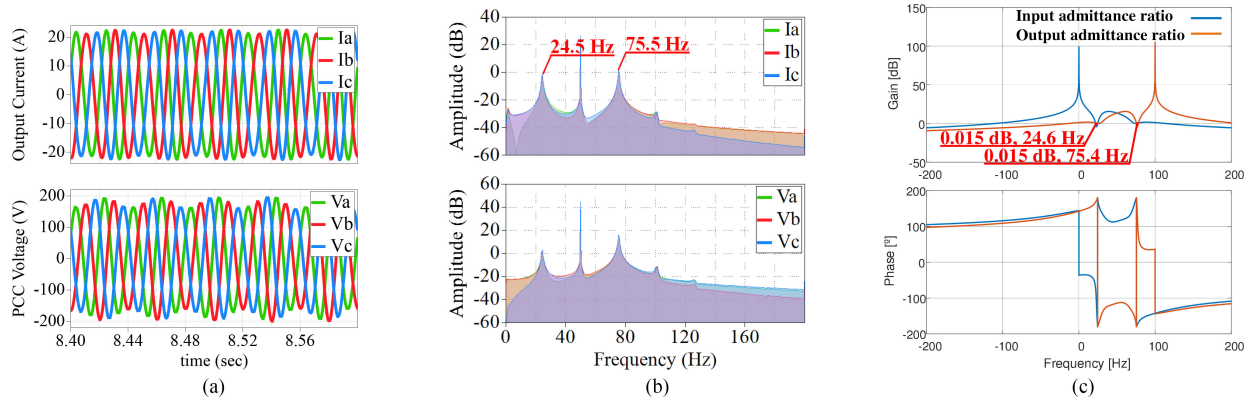


Fig. 10. Simulation result and frequency-domain analysis for Case II. (a) Converter output current and PCC voltage waveform. (b) Frequency spectrum of (a). (c) Bode plot of input and output admittance ratios.

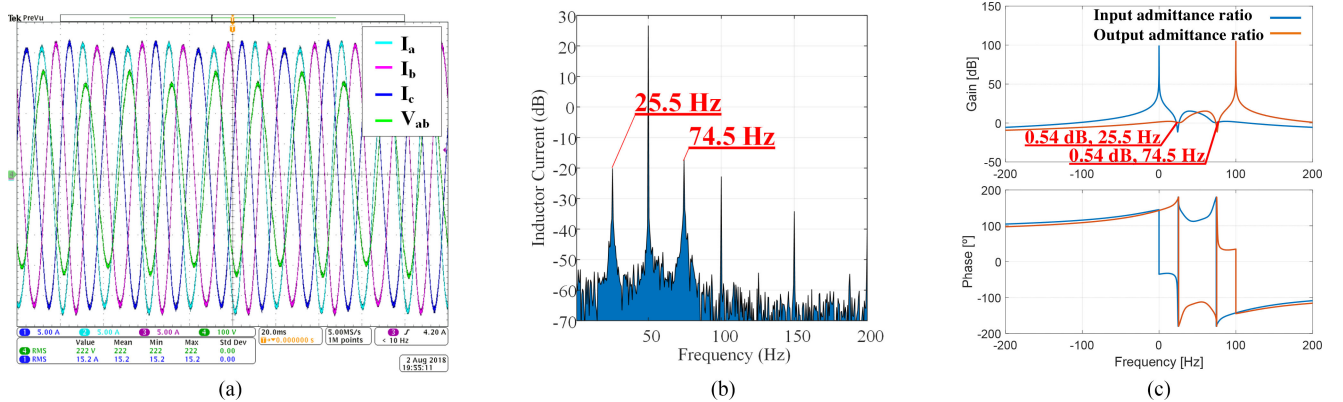


Fig. 11. Experimental result and frequency-domain analysis for Case II. (a) Converter output current and PCC voltage waveform (X-axis: 20 ms/div, Y-axis:  $I_a$ ,  $I_b$ ,  $I_c$ : 5 A/div,  $V_{ab}$ : 100 V/div). (b) Frequency spectrum of converter output current in Fig. 11(a). (c) Bode plot of input and output admittance ratios.

$50 - 25.5 = 24.5$  Hz and  $50 + 25.5 = 75.5$  Hz. Fig. 10(c) plots the frequency responses of admittances, from which the gain margin can be identified as 0.015 dB, and the phase crossover frequencies are 24.6 and 75.4 Hz, respectively.

Fig. 11 shows the experimental results and the frequency-domain analysis for the *Case II*. The critical value of  $K_{pi}$  that

makes the experimental system marginally stable is changed as 117. Yet, the same resonance frequencies as that are identified in the simulation can be observed from Fig. 11(b). Then, with the updated  $K_{pi}$ , the frequency-domain analysis result for the experimental test is shown in Fig. 11(c). It is seen that the phase crossover frequencies of two admittance ratios are 25.5 and

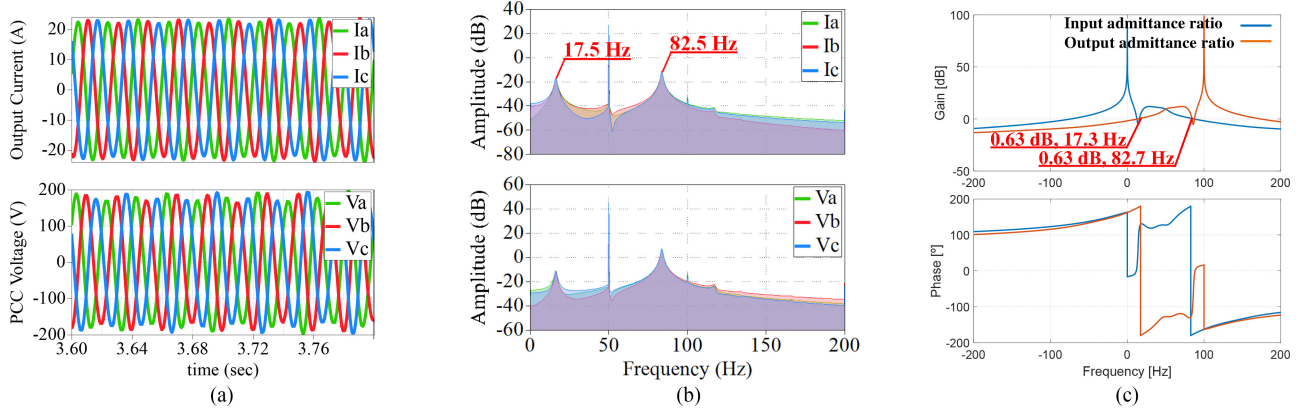


Fig. 12. Simulation result and frequency-domain analysis for Case III. (a) Converter output current and PCC voltage waveform. (b) Frequency spectrum of (a). (c) Bode plot of input and output admittance ratios.

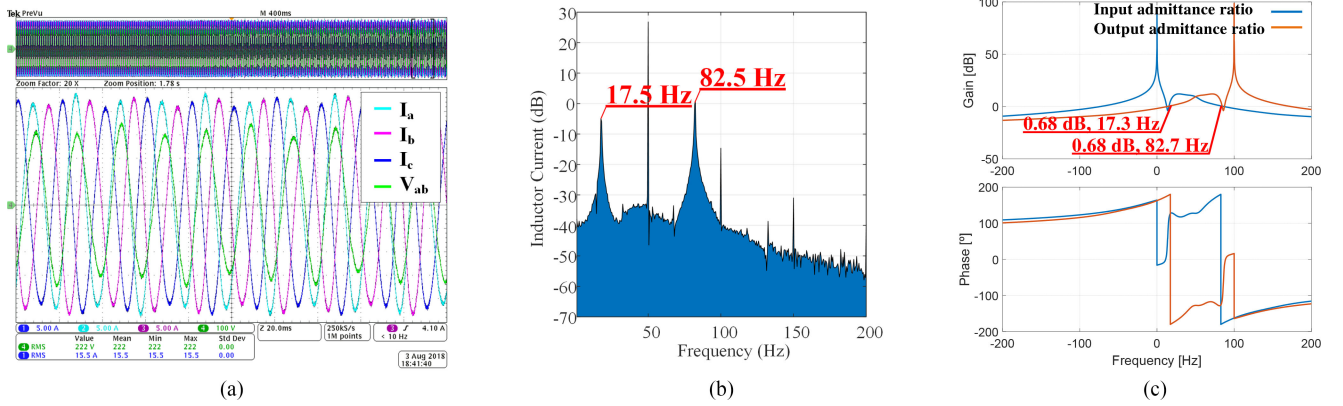


Fig. 13. Experimental result and frequency-domain analysis for Case III. (a) Converter output current and PCC voltage waveform ( $X$ -axis: 20 ms/div,  $Y$ -axis:  $I_a, I_b, I_c$ : 5 A/div,  $V_{ab}$ : 100 V/div). (b) Frequency spectrum of converter output current in (a). (c) Bode plot of input and output admittance ratios.

74.5 Hz, respectively, and their gain margin is 0.54 dB, which is higher than that in Fig. 10(c), due to the reduced  $K_{pi}$ . This case once again confirms the effectiveness of the proposed analysis method.

**Case III – Weaker Grid With Lower SCR:** Fig. 12 shows the simulation results and the associated frequency-domain analysis for the *Case III*. It is clear that the critical value of  $K_{pi}$  is reduced as 59 with the reduced SCR. Fig. 12(b) shows the harmonic spectra of the simulated voltage and current. It can be seen that the resonance frequencies are 17.5 and 82.5 Hz, which imply that a lower-frequency oscillation at the  $q$ -axis is introduced in the grid with a lower SCR. The gain margin of two admittance ratios in this case is shown in Fig. 12(c), which is 0.63 dB at the phase crossover frequencies of 17.3 and 82.7 Hz, respectively.

The experimental results and the frequency-domain analysis for the *Case III* are shown in Fig. 13, where the critical value of  $K_{pi}$  is further reduced as 56, which is slightly less than that in the simulation. The observed resonance frequencies from the harmonic spectra of the measured voltage and currents are 17.5 and 82.5 Hz, which are the same as the simulation result in Fig. 13(b). Also, the resonance frequencies identified from the frequency-domain analysis are also the same as that in Fig. 13(c),

yet the gain margin is slightly increased to 0.68 dB. Hence, the theoretical analysis results are well aligned with the simulations and experimental tests.

**Case IV – Different Grid Voltage Amplitude:** In this case, by increasing the grid voltage from 220  $V_{rms}$  to 400  $V_{rms}$ , a sequence-coupled, not only frequency-coupled, resonance phenomenon is observed. The critical value of  $K_{pi}$  that makes the system marginally stable is the same in the simulation and experiment, which is given in Table III. Fig. 14 shows the simulation result and the associated frequency-domain analysis, while the experimental result is shown in Fig. 15. It is clear that in both cases the resonance frequencies which are observed from the simulation and experiment are the same, which are 11 and 111 Hz, as shown in Figs. 14(b) and 15(b).

The frequency-domain analysis is provided in Fig. 14(c). It is clear that the phase crossover frequencies of two admittance ratios are  $-10.8$  and  $110.8$  Hz with a gain margin of 0.72 dB. This negative resonance frequency ( $-10.8$  Hz) implies a negative-sequence resonant component in the three-phase system [2]. The presence of this negative-sequence resonance is due to the oscillation induced by the PLL is 60.8 Hz in the  $q$ -axis, which, when transforming into the  $\alpha\beta$ -frame, turns as  $50 - 60.8 = -10.8$  Hz

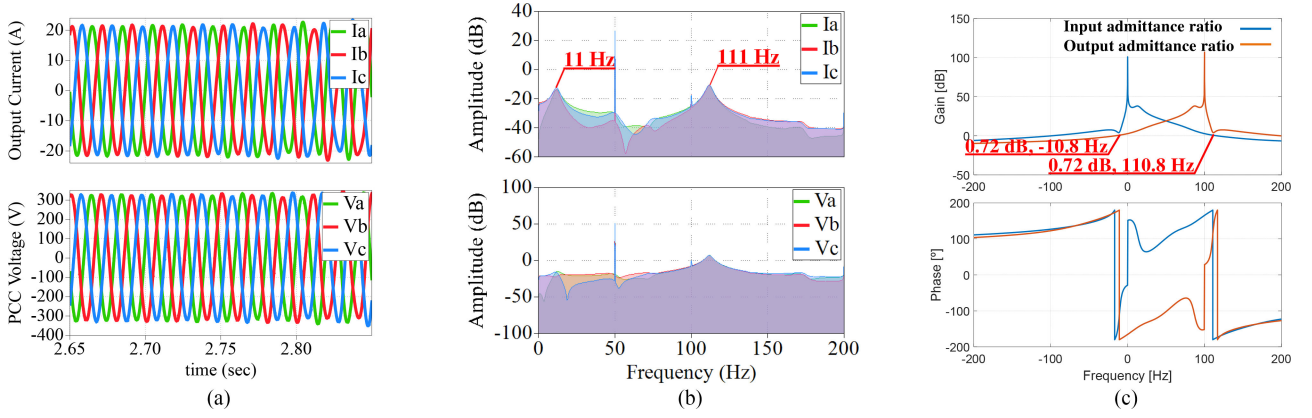


Fig. 14. Simulation result and frequency-domain analysis for Case IV. (a) Converter output current and PCC voltage waveform. (b) Frequency spectrum of (a). (c) Bode plot of input and output admittance ratios.

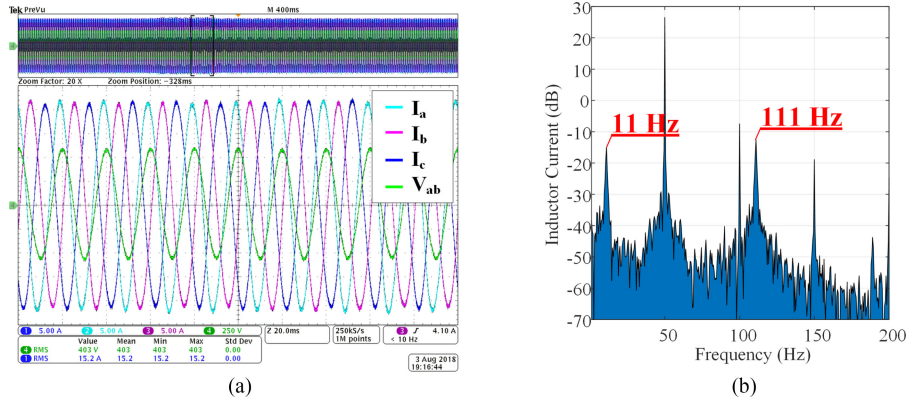


Fig. 15. Experimental result and frequency-domain analysis for Case IV. (a) Converter output current and PCC voltage waveform ( $X$ -axis: 20 ms/div,  $Y$ -axis:  $I_a, I_b, I_c$ : 5 A/div,  $V_{ab}$ : 100 V/div). (b) Frequency spectrum of converter output current in (a).

and  $50 + 60.8 = 110.8$  Hz. Since the harmonic spectra shown in Figs. 14(b) and 15(b) cannot reflect the sequence information, only the 11 and 111 Hz resonance frequencies are observed. This case study again indicates that the proposed method can also predict the sequence-coupled resonances by means of two SISO admittance ratios.

## V. CONCLUSION

In this article, a SISO system stability analysis method has been introduced for analyzing the stability of three-phase VSC systems. Differing from the conventional impedance-based approach, the proposed method utilizes the active two-port network theory to intuitively formulate a SISO open-loop gain for the MIMO dynamic system of VSCs. The SISO open-loop gain is further translated into two SISO admittance ratios and the need of measuring the four entries of the VSC admittance matrix is avoided. This superior feature significantly facilitates the system stability analysis, and the frequency-coupled resonances can be readily identified through the Bode plots of two SISO admittance ratios. Comprehensive case studies in the frequency-domain, time-domain simulations, and experimental tests have

demonstrated the effectiveness of the proposed stability analysis method.

## REFERENCES

- [1] X. Wang, F. Blaabjerg, and W. Wu, "Modeling and analysis of harmonic stability in an AC power-electronic-based power system," *IEEE Trans. Power Electron.*, vol. 29, no. 12, pp. 6421–6432, Dec. 2014.
- [2] X. Wang and F. Blaabjerg, "Harmonic stability in power electronic based power systems: Concept, modeling, and analysis," *IEEE Trans. Smart Grid*, vol. 10, no. 3, pp. 2858–2870, May 2019.
- [3] L. Harnefors, X. Wang, A. G. Yepes, and F. Blaabjerg, "Passivity-based stability assessment of grid-connected VSCs—An overview," *IEEE J. Emerg. Sel. Topics Power Electron.*, vol. 4, no. 1, pp. 116–125, Mar. 2016.
- [4] X. Wang, F. Blaabjerg, and P. C. Loh, "Passivity-based stability analysis and damping injection for multiparalleled VSCs with LCL filters," *IEEE Trans. Power Electron.*, vol. 32, no. 11, pp. 8922–8935, Nov. 2017.
- [5] L. Harnefors, "Modeling of three-phase dynamic systems using complex transfer functions and transfer matrices," *IEEE Trans. Ind. Electron.*, vol. 54, no. 4, pp. 2239–2248, Aug. 2007.
- [6] L. Harnefors, M. Bongiorno, and S. Lundberg, "Input-admittance calculation and shaping for controlled voltage-source converters," *IEEE Trans. Ind. Electron.*, vol. 54, no. 6, pp. 3323–3334, Dec. 2007.
- [7] B. Wen, D. Boroyevich, R. Burgos, P. Mattavelli, and Z. Shen, "Analysis of D-Q small-signal impedance of grid-tied inverters," *IEEE Trans. Power Electron.*, vol. 31, no. 1, pp. 675–687, Jan. 2016.



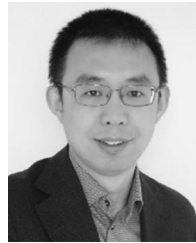
- [8] A. Rygg, M. Molinas, C. Zhang, and X. Cai, "A modified sequence-domain impedance definition and its equivalence to the dq-domain impedance definition for the stability analysis of ac power electronic systems," *IEEE J. Emerg. Sel. Topics Power Electron.*, vol. 4, no. 4, pp. 1383–1396, Dec. 2016.
- [9] M. Céspedes and J. Sun, "Impedance modeling and analysis of grid-connected voltage-source converters," *IEEE Trans. Power Electron.*, vol. 29, no. 3, pp. 1254–1261, Mar. 2014.
- [10] X. Wang, L. Harnfors, and F. Blaabjerg, "Unified impedance model of grid-connected voltage-source converters," *IEEE Trans. Power Electron.*, vol. 33, no. 2, pp. 1775–1787, Feb. 2018.
- [11] M. K. Bakhshizadeh *et al.*, "Couplings in phase domain impedance modeling of grid-connected converters," *IEEE Trans. Power Electron.*, vol. 31, no. 10, pp. 6792–6796, Oct. 2016.
- [12] D. Lu, X. Wang, and F. Blaabjerg, "Impedance-based analysis of dc-link voltage dynamics in voltage-source converters," *IEEE Trans. Power Electron.*, vol. 34, no. 4, pp. 3973–3985, Apr. 2019.
- [13] B. Wen, D. Boroyevich, R. Burgos, P. Mattavelli, and Z. Shen, "Small-signal stability analysis of three-phase ac systems in the presence of constant power loads based on measured d-q frame impedances," *IEEE Trans. Power Electron.*, vol. 30, no. 10, pp. 5952–5963, Oct. 2015.
- [14] H. Zhang, X. Wang, L. Harnfors, H. Gong, J.-P. Hasler, and H.-P. Nee, "SISO transfer functions for stability analysis of grid-connected voltage-source converters," *IEEE Trans. Ind. Appl.*, vol. 55, no. 3, pp. 2931–2941, May–Jun. 2019.
- [15] W. Egan, *Practical RF System Design*. Hoboken, NJ, USA: Wiley, 2004.
- [16] W. Ren and E. Larsen, "A refined frequency scan approach to sub-synchronous control interaction (SSCI) study of wind farms," *IEEE Trans. Power Syst.*, vol. 31, no. 5, pp. 3904–3912, Sep. 2016.
- [17] S.-K. Chung, "Phase-locked loop for grid-connected three-phase power conversion systems," *IEEE Proc. Electric Power Appl.*, vol. 147, no. 3, pp. 213–219, May 2000.
- [18] D. VandeSype, K. DeGusseme, F. DeBelie, A. VandenBossche, and J. Melkebeek, "Small-signal z-domain analysis of digitally controlled converters," *IEEE Trans. Power Electron.*, vol. 21, no. 2, pp. 470–478, Mar. 2006.
- [19] J. Undrill and T. Kostyniak, "Subsynchronous oscillations part I: Comprehensive system stability analysis," *IEEE Trans. Power Appr. Syst.*, vol. 95, no. 4, pp. 1446–1455, Jul. 1976.
- [20] W. Chen, *Active Network Analysis* (Advanced Series in Electrical and Computer Engineering). Singapore: World Scientific, 1991.



**Shih-Feng Chou** (S'09–M'17) received the B.S. and M.S. degrees in electrical engineering from National Tsing Hua University, Hsinchu, Taiwan, in 2009 and 2011, respectively. He is currently working toward the Ph.D. degree at the Department of Energy Technology, Aalborg University, Aalborg, Denmark.

He had performed R&D in power electronics for renewable energy systems with Delta Electronics Inc., Taoyuan, Taiwan, from 2012 to 2017. Since 2017, he was a Research Assistant with the Department of Energy Technology, Aalborg University. His

research focuses on modeling of large-scale power electronics based power system.



**Xiongfei Wang** (S'10–M'13–SM'17) received the B.S. degree from Yanshan University, Qinhuangdao, China, and the M.S. degree from Harbin Institute of Technology, Harbin, China, both in electrical engineering, in 2006 and 2008, respectively, and the Ph.D. degree in energy technology from Aalborg University, Aalborg, Denmark, in 2013.

Since 2009, he has been with the Department of Energy Technology, Aalborg University, where he became Assistant Professor in 2014, an Associate Professor in 2016, and a Professor and Research Program Leader for Electronic Power Grid (eGrid) in 2018. His current research interests include modeling and control of grid-interactive power converters, stability, and power quality of power electronic based power systems, active, and passive filters.

Dr. Wang was selected into Aalborg University Strategic Talent Management Program in 2016. He serves as an Associate Editor for the IEEE TRANSACTIONS ON POWER ELECTRONICS, the IEEE TRANSACTIONS ON INDUSTRY APPLICATIONS, and the IEEE JOURNAL OF EMERGING AND SELECTED TOPICS IN POWER ELECTRONICS. He received six IEEE Prize Paper Awards, the 2017 Outstanding Reviewer Award of IEEE TRANSACTIONS ON POWER ELECTRONICS, the 2018 IEEE Power Electronics Society (PELS) Richard M. Bass Outstanding Young Power Electronics Engineer Award, and the 2019 IEEE PELS Sustainable Energy Systems Technical Achievement Award.



**Frede Blaabjerg** (S'86–M'88–SM'97–F'03) was with ABB-Scandia, Randers, Denmark, from 1987 to 1988. From 1988 to 1992, he received the Ph.D. degree in electrical engineering at Aalborg University, Aalborg, Denmark, in 1995.

He became an Assistant Professor in 1992, an Associate Professor in 1996, and a Full Professor of power electronics and drives in 1998. From 2017 he became a Villum Investigator. He is honoris causa at University Politehnica Timisoara (UPT), Romania, and Tallinn Technical University (TTU) in Estonia.

He has authored or coauthored more than 600 journal papers in the fields of power electronics and its applications. He is the Co-Author of four monographs and Editor of ten books in power electronics and its applications. His current research interests include power electronics and its applications such as in wind turbines, PV systems, reliability, harmonics, and adjustable speed drives.

He was the Editor-in-Chief for the IEEE TRANSACTIONS ON POWER ELECTRONICS from 2006 to 2012. He has been a Distinguished Lecturer for the IEEE Power Electronics Society from 2005 to 2007 and for the IEEE Industry Applications Society from 2010 to 2011 as well as from 2017 to 2018. In 2019–2020 he serves as the President of IEEE Power Electronics Society. He is the Vice-President of the Danish Academy of Technical Sciences too. He was nominated in 2014–2018 by Thomson Reuters to be among the 250 most cited researchers in engineering in the world. He has received 31 IEEE Prize Paper Awards, the IEEE PELS Distinguished Service Award in 2009, the EPE-PEMC Council Award in 2010, the IEEE William E. Newell Power Electronics Award 2014, the Villum Kann Rasmussen Research Award 2014, and the Global Energy Prize in 2019.